

MDPI

Article

# Prediction of Large Second Harmonic Generation in the Metal-Oxide/Organic Hybrid Compound CuMoO<sub>3</sub>(p2c)

Tingting Yang <sup>1,2</sup>, Xueli Huang <sup>1,2</sup>, Xiyue Cheng <sup>2,3</sup>,\*, Paul A. Maggard <sup>4</sup>, Myung-Hwan Whangbo <sup>2,4</sup>, Chengkai Luan <sup>2,5</sup> and Shuiquan Deng <sup>2,3</sup>,\*

- College of Chemistry, Fuzhou University, Fuzhou 350116, China; yangting@fjirsm.ac.cn (T.Y.); huangxueli@fjirsm.ac.cn (X.H.)
- State Key Laboratory of Structural Chemistry, Fujian Institute of Research on the Structure of Matter (FJIRSM), Chinese Academy of Sciences (CAS), Fuzhou 350002, China; whangbo@ncsu.edu (M.-H.W.); ckluan@fjirsm.ac.cn (C.L.)
- <sup>3</sup> Fujian Science and Technology Innovation Laboratory for Optoelectronic Information of China, Fuzhou 350108, China
- Department of Chemistry, North Carolina State University, Raleigh, NC 27695-8204, USA; pamaggar@ncsu.edu
- College of Physics and Energy, Fujian Normal University, Fuzhou 350117, China
- \* Correspondence: xycheng@fjirsm.ac.cn (X.C.); sdeng@fjirsm.ac.cn (S.D.)

**Abstract:** Noncentrosymmetric hybrid framework (HF) materials are an important system in discovering new practical second-order nonlinear optical materials. We calculated the second harmonic generation (SHG) response of a noncentrosymmetric (NCS) organic–inorganic HF compound, CuMoO<sub>3</sub>(p2c) (p2c = pyrazine-2-carboxylate) to find that it exhibits the largest SHG response among all known NCS HF materials with one-dimensional helical chains. Further atom response theory analysis revealed that the metal atoms Cu and Mo contribute much more strongly than do nonmetal atoms in determining the strength of the SHG response, which is a novel example in nonlinear optical materials known to date.

Keywords: nonlinear optical material; noncentrosymmetric; MOF; atom response theory; DFT calculation



Citation: Yang, T.; Huang, X.; Cheng, X.; Maggard, P.A.; Whangbo, M.-H.; Luan, C.; Deng, S. Prediction of Large Second Harmonic Generation in the Metal-Oxide/Organic Hybrid Compound CuMoO<sub>3</sub>(p2c). Symmetry 2022, 14, 824. https://doi.org/10.3390/sym14040824

Academic Editor: Enrico Bodo

Received: 22 March 2022 Accepted: 11 April 2022 Published: 14 April 2022

**Publisher's Note:** MDPI stays neutral with regard to jurisdictional claims in published maps and institutional affiliations.



Copyright: © 2022 by the authors. Licensee MDPI, Basel, Switzerland. This article is an open access article distributed under the terms and conditions of the Creative Commons Attribution (CC BY) license (https://creativecommons.org/licenses/by/4.0/).

# 1. Introduction

Nonlinear optical (NLO) crystals play a vital role in modern laser technologies and sciences due to their ability to convert the frequency of an incident laser beam through the second harmonic generation (SHG) process [1–5]. A noncentrosymmetric (NCS) arrangement of atoms is a prerequisite for the generation of non-zero second-order NLO properties in bulk materials. The search for new NCS structures with excellent SHG properties remains a hot scientific challenge. Although there exist a number of extensively studied and commercially available inorganic NLO crystals, there has been tremendous interest in finding new NLO materials in other systems such as organic molecular crystals, inorganic-organic hybrid nanocomposites, self-assembled chromophoric superlattices and inorganic-organic hybrid framework materials (including both nanoporous metal-organic frameworks (MOFs) and dense inorganic-organic frameworks (IOFs)) [6-10]. Hybrid framework materials are constructed by employing modular synthetic procedures with metal ions (i.e., Zn<sup>2+</sup>, Cd<sup>2+</sup>, Mn<sup>2+</sup>, Ag<sup>+</sup>, Cu<sup>+</sup>) or inorganic nodes (i.e., metal-oxide, metalfluoride, metal-chalcogenides and metal-halides) that are covalently and/or coordinately bonded to various organic linkers. Because of the advantages over conventional inorganic materials (e.g., structural tunability at a molecular level, chemical stability, and ease of synthesis on a large bulk scale), NCS hybrid framework materials are expected to form a new class of potentiality practical NLO materials [11–13].

Numerous hybrid framework materials have been reported to be SHG-active. According to the dimensionality of the coordination networks, they can be roughly classified

Symmetry 2022, 14, 824 2 of 11

into three groups: (a) three-dimensional (3D) networks (e.g., diamondoid, octupolar), (b) two-dimensional (2D) grid structures, and (c) one-dimensional (1D) chains (e.g., helical chains). Lin et al. suggested that 3D and 2D networks with a high degree of controllability and predictability are better platforms for the synthesis of NCS MOFs [6,8], and they reported a number of MOFs with a large SHG response, which includes Cd{3-[2-(4-pyridyl)ethenyl]benzoate}<sub>2</sub> (powder SHG intensity  $I_{powder}^{2\omega}$  of  $800 \times \alpha$ -SiO<sub>2</sub>, Fdd2) [14] and other systems [15]. For hybrid framework materials, the molecular origin of SHG is believed to arise from the electronic asymmetry (push-pull effect or acceptor-donor effect) induced by the polarization of ligand electron density or the metal-to-ligand/ligand-tometal charge transfer [6,9,10,16]. The alignment of NLO chromophores may be necessary for NCS hybrid framework materials to have a large SHG response. For example, Ye et al. obtained a zinc MOF based on a 2D square grid network, in which the ligands involve an aligned two-center acceptor-donor system, which displays a very strong SHG response ( $I_{\text{powder}}^{2\omega}$  of 50 × urea and 500 × KH<sub>2</sub>PO<sub>4</sub> (KDP), respectively) [16]. Yu et al. encapsulated a matching ordered organic dipolar chromophore in the pores of porous MOFs forming a highly NLO active anionic MOF (ZJU-28 $\subset$ DPASD,  $I_{\rm powder}^{2\omega}$  of 18.3  $\times$   $\alpha$ -SiO<sub>2</sub>) [17]. However, the NCS hybrid framework materials with 1D helical chains are not known to have large SHG responses, although it may be related to synthetic difficulty and unpredictability. Maggard et al. used short organic ligands to bridge polar or chiral inorganic basic building units (i.e., MoO<sub>2</sub>F<sub>4</sub><sup>2-</sup>) to obtain two isomorphic SHG-active NCS solids with helical chains [18,19],  $A(pyz)(H_2O)_2MoO_2F_4$  (A = Zn, Cd, pyz = pyrazine,  $I_{\rm powder}^{2\omega}$  of ~0.28–1  $\times$   $\alpha$ -SiO<sub>2</sub>,  $P3_2$ 21). Other examples with 1D helical chains include  $Cu(pzc)_2AgReO_4$  (pzc = pyrazinecarboxylate,  $I_{powder}^{2\omega}$  of ~0.5–0.7 ×  $\alpha$ -SiO<sub>2</sub>,  $P4_32_12$ ) [20],  $[Zn(mpz)_3]_2[MoO_2F_4]_2$  (mpz = 3-methylpyrazole,  $I_{powder}^{2\omega}$  of ~10 ×  $\alpha$ -SiO<sub>2</sub>,  $PnaO_1$ ) [21], and [(S)-C<sub>5</sub>H<sub>14</sub>N<sub>2</sub>][(MoO<sub>3</sub>)<sub>3</sub>(SO<sub>4</sub>)]·H<sub>2</sub>O ( $I_{powder}^{2\omega}$  of ~5 ×  $\alpha$ -SiO<sub>2</sub>,  $Pna2_1$ ) [22]. The cancellation or the absence of a net dipole moment in these structures is usually considered to be responsible for their low SHG response [19]. Finding hybrid framework materials with 1D helical chains possessing a large SHG response remains a challenge. It should be pointed out that the SHG phenomenon, as a second-order polarization, involves both the occupied and the unoccupied states of a material, while the vector sum of the dipole moments of the groups within a unit cell, as a zero-order polarization, associated with only the occupied states. The non-zero vector sum of the dipole moments lead to a polar structure which guarantees the presence of an NCS structure, which is a necessary condition for the occurrence of the SHG phenomenon, but it does not influence the magnitude of the second-order NLO properties. It is desirable to understand the SHG responses for the NCS hybrid framework compounds at the electronic and the atomic levels.

Recently, Luo et al. [23] reported a new NCS metal-oxide/organic hybrid compound CuMoO<sub>3</sub>(p2c) (p2c = pyrazine-2-carboxylate) with 1D helical chains. However, so far neither theoretical nor experimental work on the linear and the nonlinear optical properties of this compound has been reported. Based on our first-principles calculation, we found CuMoO<sub>3</sub>(p2c) exhibits a very strong SHG response with a static effective SHG value  $d_{eff}^p$  calculated to be 30.6 pm/V. This value is about 92.7 times that of KDP (~927 ×  $\alpha$ -SiO<sub>2</sub>, 3.12 × AgGaS<sub>2</sub> (AGS)), which ranks the SHG response of CuMoO<sub>3</sub>(p2c) to be the highest among all the reported hybrid framework materials with 1D helical chains. Besides, our atom response theory (ART) analysis [24] shows that the SHG response of CuMoO<sub>3</sub>(p2c) originates largely from the states of the metal ions, Cu<sup>+</sup> and Mo<sup>6+</sup>, i.e., approximately 56% of the total SHG response. Such a large contribution from metal ions also makes CuMoO<sub>3</sub>(p2c) a quite special example in NLO materials.

# 2. Materials and Methods

Computational Details

**VASP calculations.** The structural and the electronic properties of  $CuMoO_3(p2c)$  were calculated within the framework of density functional theory (DFT) [25,26] by using the

Symmetry **2022**, 14, 824 3 of 11

Vienna ab-initio simulation package (VASP) [27-29] with the projector augmented wave (PAW) method [30]. The generalized gradient approximation (GGA) within the Perdew-Burke-Ernzerhof (PBE)-type exchange-correlation potentials [31] was used throughout this work. The employed PAW-PBE pseudopotentials [32] with 11  $(3d^{10}4s^1)$ , 14  $(4s^24p^64d^55s^1)$ , 6  $(2s^22p^4)$ , 5  $(2s^22p^3)$ , 4  $(2s^22p^2)$  and 1  $(1s^1)$  valence electrons for Cu, Mo, O, N, C, and H were used to describe the electron-ion interactions, respectively. The plane wave cutoff energy for the expansion of wave functions was set at 600 eV and the tetrahedron method with Blöchl corrections was used for integrations. The numerical integrations in the Brillouin zones were performed by utilizing  $7 \times 7 \times 4$  Monkhorst–Pack k-point mesh, which showed an excellent convergence of the energy differences (0.005 eV) and stress tensors (0.001 eV/Å). The quasi-Newton algorithm as implemented in the VASP code was used in all structural relaxations. In this work, both the cell volume and the atomic positions were all allowed to relax to minimize the internal forces. The optimized lattice parameters, a = 7.791 Å and c = 11.229 Å, are slightly overestimated with respect to the experimental, which were measured at room temperature as usual with the PBE functional. Details of the optimized structure and the agreement with the experimental values are given in Table S1 of the Supporting Information.

In our calculations for the linear and the nonlinear optical properties, we employed the sum over states (SOS) method [33–35] using the code we developed [24] based on the calculated electronic structures from the VASP optical module. The SOS formalism for second-order susceptibility was derived by Aversa and Sipe [33] and later modified by Rashkeev et al. [34,36] and Sharma et al. [35,37]. To gain insight into the origin of SHG response, the contributions  $A_{\tau}$  of the individual atoms  $\tau$  to a specific component, e.g., the largest, of the total SHG response tensor, were determined by performing atom response theory (ART) analysis [24,38] for the CuMoO<sub>3</sub>(p2c) structure. Note that, the chirality may lead to higher-order interactions beyond the electric dipole approximation, for which one needs to use model studies instead of the first-principles method [39].

**Partial response functional (PRF) method.** The contribution of a certain occupied energy region between  $E_B$  and valence band maximum (VBM),  $\zeta_V(E_B)$ , to each SHG coefficient  $d_{il} = \frac{1}{2}\chi_{ijk}^{(2)}$ , l = 1, 2, 3, 4, 5, 6 is determined by considering only those excitations from all occupied states between  $E_B$  and VBM to all the unoccupied states of the conduction bands (CBs) and the contribution,  $\delta\zeta_V(E_B)$ , of specific occupied states of energy  $E_B$  to each  $d_{il}$  by the excitations from that energy to all unoccupied states of the CBs.

$$\delta \zeta_V(E_B) = -\frac{d\zeta_V(E_B)}{dE_B} \tag{1}$$

Similarly, the contribution,  $\zeta_C(E_B)$ , of a certain unoccupied region between the conduction band minimum (CBM) and  $E_B$  to each  $d_{il}$  is determined by the excitations from all occupied states of the VBs only to all unoccupied states between CBM and  $E_B$ , and the contribution,  $\delta\zeta_C(E_B)$ , of specific unoccupied states of energy  $E_B$  to each  $d_{il}$  by the excitations from all occupied states of the VBs only to that energy.

$$\delta \zeta_C(E_B) = \frac{d\zeta_C(E_B)}{dE_B} \tag{2}$$

Atom response theory (ART) analysis. To evaluate the individual atom contributions to the SHG components,  $d_{il}$ , it is computationally more convenient to express the corresponding PRFs in terms of the band index  $I_B$ ,  $\zeta(I_B)$ , where the band index  $I_B$  runs from 1 to  $N_{tot}$  (i.e., the total number of band orbitals) with increasing energy,  $E_B$ , from  $E_{min}$  to  $E_{max}$ . Here,  $\zeta_V(I_B)$  and  $\zeta_C(I_B)$  are denoted as  $V^B\zeta_j$  and  $V^B\zeta_j$ , respectively, with  $V^B\zeta_j$  replaced by a subscript  $V^B\zeta_j$ .

Symmetry **2022**, 14, 824 4 of 11

Suppose that a specific atom  $\tau$  has L atomic orbitals with a coefficient  $\stackrel{VB}{C}_{L\tau}^{\stackrel{j}{k}j}$  in the valence band j at a wave vector  $\stackrel{\rightarrow}{k}$ . The total contribution  $\stackrel{VB}{A}_{\tau}$  of an atom  $\tau$  makes to the SHG coefficient from all the VB bands j is written as

$${}^{VB}A_{\tau} = \frac{\Omega}{(2\pi)^3} \int d\overset{\rightarrow}{k} \cdot \sum_{L,i} {}^{VB}\zeta_j \left| {}^{VB}C_{L\tau}^{\overset{\rightarrow}{k}j} \right|^2 \tag{3}$$

where  $\Omega$  is the unit cell volume,  ${}^{VB}\zeta_j$  is the corresponding PRFs in terms of the band index j. Similarly, the total contribution  ${}^{CB}A_{\tau}$  of an atom  $\tau$  makes to the SHG coefficient from all the CB bands j is written as

$${}^{CB}A_{\tau} = \frac{\Omega}{(2\pi)^3} \int d\vec{k} \cdot \sum_{L,j} {}^{CB}\zeta_j \left| {}^{CB}C_{L\tau}^{\vec{k}j} \right|^2 \tag{4}$$

in which we assumed that the atom has L atomic orbitals with coefficient  ${}^{CB}C_{L\tau}^{\vec{k}j}$  in the conduction band j at a wave vector  $\vec{k}$ . To calculate the actual contribution of each constituent atom in a unit cell to the total SHG response, one needs to consider the signs of  ${}^{VB}\zeta_j$  and  ${}^{CB}\zeta_j$ .

The total contribution,  $A_{\tau}$ , each individual atom makes to the SHG response from both the VBs and the CBs (i.e., from all the bands) is given by

$$A_{\tau} = \frac{\left({}^{VB}A_{\tau} + {}^{CB}A_{\tau}\right)}{2} \tag{5}$$

where the factor of 1/2 is applied to remove the double-counting of each excitation.

#### 3. Results and Discussion

## 3.1. Structure

The Cu/Mo-oxide CuMoO<sub>3</sub>(p2c) crystallizes in the NCS space group P3<sub>2</sub> (Figure 1 and Table S1). Within each unit cell, Cu and Mo atoms each have one crystallographically unique site, whereas the O, N, C, and H atoms occupy five, two, five and three independent crystallographic positions, respectively. All atoms are at special Wyckoff positions of 3a. The Mo atoms are coordinated with five O atoms (O1, O3, O4, O4, O5) and one N1 atom, forming a distorted MoO<sub>5</sub>N octahedron with Mo-O and Mo-N bond lengths around 1.92 and 2.37 Å, respectively. Neighbouring Mo-centered octahedra are connected by sharing the O4 atom with alternating short (1.82 Å) and long (2.12 Å) Mo-O4 bond distances as well as alternating small ( $\angle$ Mo-O4-Mo = 145.64°) and large ( $\angle$ O4-Mo-O4 = 162.57°) bond angles forming 1D zigzag -Mo-O-Mo-O- chains along the c-axis (Figure 1a). Besides, this zigzag chain propagates along the 32 screw axis, that is, the MoO5N octahedron could duplicate itself by rotating  $120^{\circ}$  within the ab plane and gliding 2c/3 along the c axis. In addition, the Cu atoms form a distorted CuO<sub>3</sub>N tetrahedron with the surrounding three O atoms (O2, O3, O5) and one N2 atom with the Cu-O and Cu-N distances of ~2.03 Å and ~1.99 Å, respectively. Each CuO<sub>3</sub>N tetrahedra is corner shared with two neighbouring MoO<sub>5</sub>N octahedra through the O3 and O5 atoms, forming the inorganic CuMoO<sub>3</sub> helical chains. Further, the N1 and O1 atoms from one p2c ligand simultaneously coordinate with the Mo atom, while the O2 and N2 atoms from two different p2c ligands connect the Cu atoms (Figure 1b). Thus, the 3D inorganic-organic hybrid network is constructed through the bridging p2c ligands. Note that, the Mo-O1 and the Cu-O2 distances (2.16 and 2.08 Å) connecting to the p2c ligands are slightly longer than the other Mo-O and Cu-O bonding lengths (1.86 and 2.01 Å) within each MoO<sub>5</sub>N octahedra and CuO<sub>3</sub>N tetrahedra, respectively. This fact reflects that the metal/ligand interaction is relatively weak compared with the interaction within the inorganic framework.

Symmetry **2022**, 14, 824 5 of 11

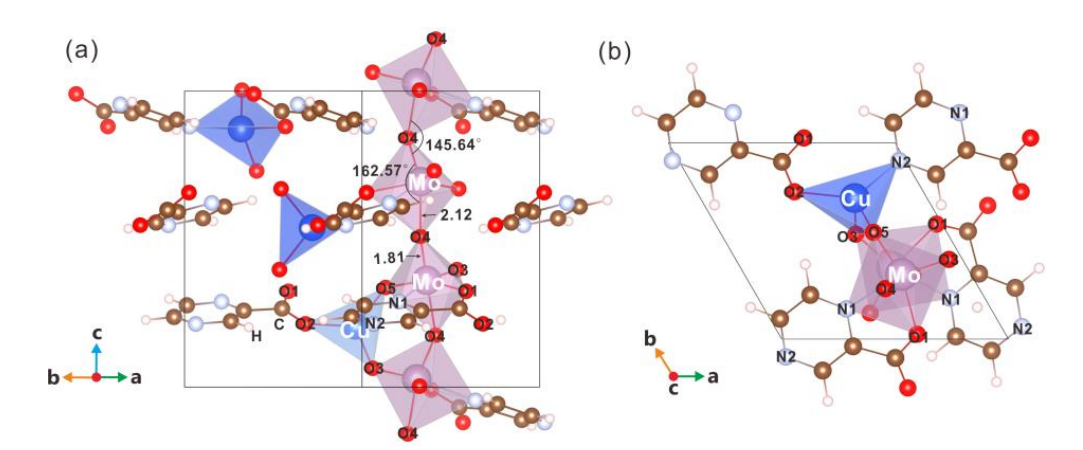


**Figure 1.** (a) Crystal structure of  $CuMoO_3(p2c)$  illustrating the  $CuMoO_3$  helical chain. (b) Local coordination environment between the p2c ligand and the inorganic framework of  $CuMoO_3(p2c)$ .

#### 3.2. Electronic Structures

Our electronic calculations reveal that  $CuMoO_3(p2c)$  has a small indirect bandgap  $(E_g^{PBE})$  of 0.743 eV, which is smaller than the experimentally measured  $(E_g^{exp}=1.32 \text{ eV})$ . In computing optical properties, this deficiency of the DFT [26] is often corrected empirically by employing the scissor operation [40] in which the conduction bands (CBs) are shifted in energy to have the experimental bandgap [41,42]. The calculated density of states (DOS) and electronic band structure (Figures 2a and S1–S4) show that the top portion of valence bands (VBs)  $(-1.0 \text{ eV} \text{ to } E_F)$  is dominated by the Cu-3d orbitals, while the O-2p orbitals occupy the relatively lower energy range (-6.0 to -1.8 eV). The bottom part of the conduction bands (CBs)  $(E_g$ -7 eV) is primarily made up of the Mo-4d, C-2p, and N-2p states, while the antibonding states involving the 2p states of the O, C, N atoms are found in the energy range between 7 to 25 eV.

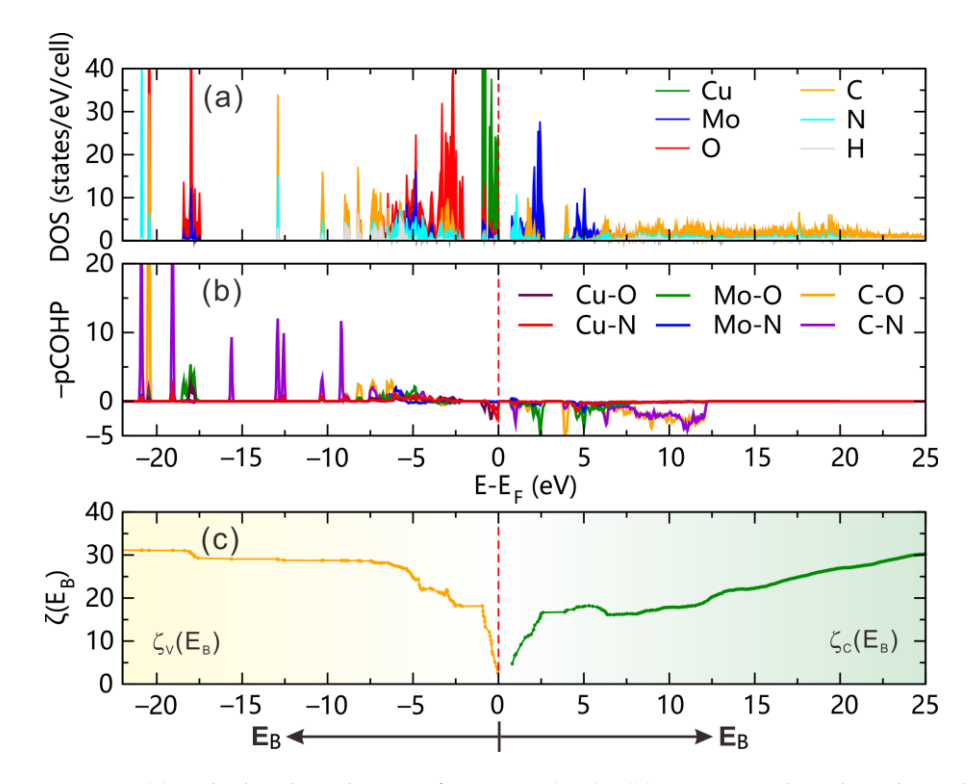


**Figure 2.** (a) Calculated total DOS of CuMoO<sub>3</sub>(p2c). (b) –pCOHP plots describing the average chemical bonding interactions. (c)  $\zeta_V(E_B)$ -vs- $E_B$  plot (left) and  $\zeta_C(E_B)$ -vs- $E_B$  plot (right) calculated for the largest SHG component d<sub>11</sub> of CuMoO<sub>3</sub>(p2c). The values are in pm/V.

Symmetry **2022**, 14, 824 6 of 11

The crystal orbital Hamilton population (COHP) [43,44] analysis (Figure 2b) shows that the frontier orbital states (-4.4 eV to  $E_F$ ) are described mainly by nonbonding states made up of Cu-3d and O-2p orbitals with a small mixture of weak Cu-O/N d-p antibonding states (Figure S2). Generally, these filled nonbonding and antibonding states near  $E_F$  are highly polarizable and hence are important for the optical properties. Besides, some O-2p and N-2p states make weak bonding interaction with Mo-4d and Cu-3d states as well as C-2p orbitals around -9.0 to -4.4 eV, leading to a dispersive orbitals feature. Strong Cu-O and Mo-O s-p bonding interaction can be found at around -18 eV. The covalent character of the C-O/N bonds is much stronger than that of the Mo-O/N and the Cu-O/N bonds (Figure 2b).

## 3.3. Optical Properties

Calculations of the refractive indices ( $n_0$  and  $n_e$ ) as a function of wavelength (Figure 3) reveal that CuMoO<sub>3</sub>(p2c) can meet the Type-I phase matching condition at  $\lambda = 1.88$  µm, a value in the IR range. Besides, the calculated birefringence value  $\Delta n$  for CuMoO<sub>3</sub>(p2c) is 0.21 at 1910 nm (Figure S5). Such a large birefringence reflects a strong optical anisotropy of CuMoO<sub>3</sub>(p2c). The value of  $\Delta n$  in a uniaxial optical material is the difference between  $n_0$  and  $n_e$ ,  $\Delta n = |n_0 - n_e|$ . As  $n_0 > n_e$  in CuMoO<sub>3</sub>(p2c), it is a negative uniaxial crystal.

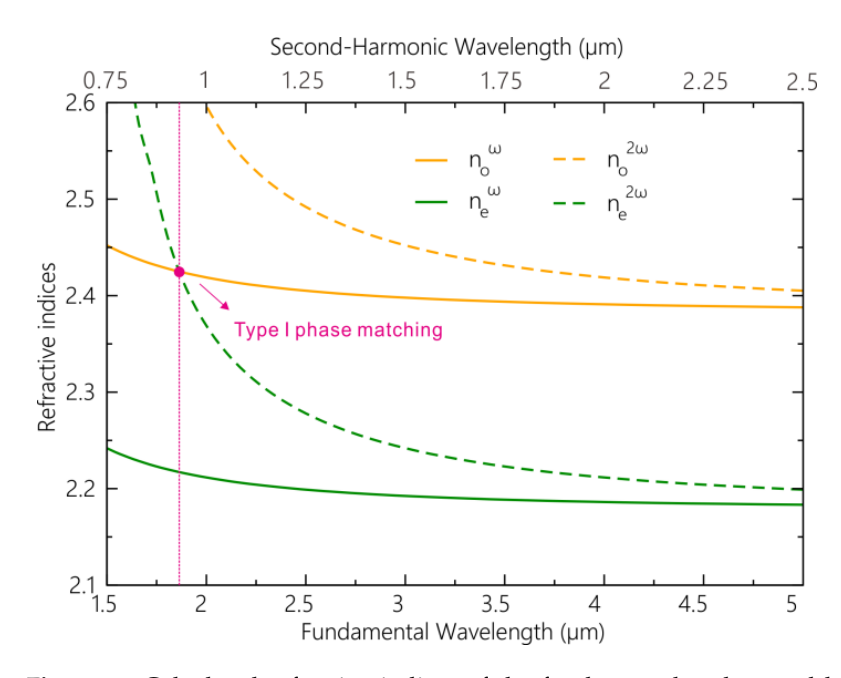


**Figure 3.** Calculated refractive indices of the fundamental and second harmonic wavelengths for CuMoO<sub>3</sub>(p2c). The pink point represents the meet of Type I phase-matching condition  $(n_e(2\omega) = n_o(\omega))$  for negative uniaxial crystals.

Due to the point group of 3, the SHG tensor of CuMoO<sub>3</sub>(p2c) has 13 non-zero components, in which 5 of them are independent, i.e.,  $d_{11} = -d_{12} = -d_{25}$ ,  $d_{22} = -d_{21} = -d_{16}$ ,  $d_{31} = d_{32} = d_{24} = d_{15}$ ,  $d_{14} = -d_{25}$  and  $d_{33}$ , as presented in Table S2. As the Kleinman symmetry, i.e.,  $d_{14} = -d_{25} = 0$ , is not followed in CuMoO<sub>3</sub>(p2c), it was not enforced in calculating the NLO properties in this work. The effective  $d_{eff}^p$ , an average SHG coefficient over all possible orientations of the powder crystals, is estimated from the formula derived by Kurtz-Perry [45] and Cyvin et al. [46] based on the calculated non-zero SHG tensors. The static effective SHG value of CuMoO<sub>3</sub>(p2c) is calculated to be 30.6 pm/V, which is about 3.12 times that of commercial AGS (static  $d_{eff}^{AGS} = 9.8$  pm/V) and 92.7 times that of KDP (static  $d_{eff}^{KDP} = 0.33$  pm/V). At the wavelength of 1910 nm (~0.65 eV), the  $d_{eff}^p$  value of CuMoO<sub>3</sub>(p2c) is predicted to be 121.35 pm/V, i.e., ~8.20 ×  $d_{eff}^{AGS}$  ( $d_{eff}^{AGS} = 14.8$  pm/V at 1910 nm). We have tried to estimate the  $d_{eff}$  for large crystals using Midwinter et al.'s

Symmetry **2022**, 14, 824 7 of 11

method [47] and obtained a maximum value of ~168.7 pm/V at  $\theta = 0.0^{\circ}$  and  $\phi = 45.0^{\circ}$ at  $\omega = 1910$  nm, which is larger than the powder  $d_{eff}^p$ . Using the d<sub>eff</sub> and the refractive indices, one can get a much larger figure of merit value [48] ( $FOM = d_{eff}^2/(n(\omega)^2 n(2\omega))$ , ~2058.7  $(pm/V)^2$  than that 150  $(pm/V)^2$ , of LiNbO<sub>3</sub>, which suggests a great potential value of CuMoO<sub>3</sub>(p2c)—though the large crystal has not yet been obtained. We also calculated the SHG responses for several NCS hybrid framework compounds with helical chains, as presented in Table S2, which also lists the available experimental SHG values. Clearly, CuMoO<sub>3</sub>(p2c) has the highest  $d_{eff}^p$  value among all reported NCS hybrid framework materials with helical chains. This remarkably strong SHG response is larger than those found in the majority of hybrid framework materials reported to date. Only a few are exceptional:  $[Cd(L-N_3)_2(H_2O)_2]_n$  ( $I_{powder}^{2\omega}$  of 80 × urea) [49], Zn((E)-4pyv-3-bza)<sub>2</sub> ( $I_{powder}^{2\omega}$  of 1000 ×  $\alpha$ -SiO<sub>2</sub>) [50], and [(CN<sub>4</sub>-C<sub>6</sub>H<sub>4</sub>-C<sub>12</sub>H<sub>7</sub>N-C<sub>5</sub>H<sub>4</sub>N)<sub>2</sub>Zn]·1.5H<sub>2</sub>O  $(I_{powder}^{2\omega} \text{ of } 50 \times \text{urea})$  [16]. Besides, the SHG response of CuMoO<sub>3</sub>(p2c) is even larger than several newly reported inorganic IR-NLO crystals, e.g., Li[LiCs<sub>2</sub>Cl] [Ga<sub>3</sub>S<sub>6</sub>] ( $I_{powder}^{2\omega}$  of  $0.7 \times AGS$ ) [51],  $Ba_2SnS_5$  ( $I_{powder}^{2\omega}$  of  $1.1 \times AGS$ ) [52],  $Na_2MSn_2Se_6$  (M = Zn/Cd) (( $I_{powder}^{2\omega}$ ) of 3 and 2.2 × AGS) [53], and  $\delta$ -Ga<sub>2</sub>Se<sub>3</sub> ( $I_{powder}^{2\omega}$  of 2.3 × AGS) [54]. These facts indicate that CuMoO<sub>3</sub>(p2c) is a promising IR hybrid NLO crystal material.

## 3.4. Atom Response Theory Analyses

We investigate the origin of the SHG responses further by employing the ART analysis [24]. Shown in Figure 2c is the partial response functionals (PRFs),  $\zeta_V(E_B)$  and  $\zeta_C(E_B)$  as well as their derivatives (Figures S6 and S7),  $\delta\zeta_V(E_B)$  and  $\delta\zeta_C(E_B)$ , for CuMoO<sub>3</sub>(p2c). The  $\zeta_V(E_B)$  functional increases in magnitude with decreasing  $E_B$  from  $E_F$  to -4.4 eV indicating that the nonbonding Cu 3d and O 2p states are the dominating contributors to the SHG response in the VB part. From the rising amplitude of the  $\zeta_V(E_B)$  functional, it is clear that the contribution from the Cu 3d states ( $E_F$  to -1.0 eV) is greater than that from the O 2p states (-1.8 to -4.4 eV). This is so because the completely filled d orbitals of each Cu<sup>+</sup> ( $d^{10}$ ) possess more electrons than the completely filled 2p orbitals of each O<sup>2-</sup> (p<sup>6</sup>). However, in the energy range of -4.4 to -9.0 eV where the C-O/N, Mo-O/N and Cu-O/N bonding interaction occurs, the functional shows small variation, showing that these bonding states contribute little to the SHG response. A dramatical change from the CB minimum to 7 eV and the steady increase at the higher energy range of the  $\zeta_C(E_B)$  functional reveal the contribution from the unoccupied Mo-4d and C/O/N-2p states in the CB part.

The quantitative contribution of an individual atom  $\tau$ , A $\tau$  (in %), to the strongest SHG coefficient d<sub>11</sub> for CuMoO<sub>3</sub>(p2c) is obtained based on the PRFs. As presented in Tables 1 and S3, the A $\tau$  of Cu (~11.7%) is nearly 1.7 times that of Mo (~7.0%) and 7.3 times that of O ( $\sim$ 1.6%) and N ( $\sim$ 1.2%). Besides, the A $\tau$  value of C and H are negligibly small, <0.8%. These results reflect that the metal atoms Cu and Mo serve as the NLO-active centers at the atomic scale. Considering the number of atoms of each element in the unit cell, the total contributions of Cu, Mo, O, N, C, and H are 35.2, 20.9, 24.1, 7.4, 11.1, and 1.4%. Although the uneven stoichiometry effect is included, the metal atom Cu is still the leading contributor to the SHG response, while the contributions from the Mo and O atoms are comparable. This further reflects the important contribution from the metal atoms since the number of O in a unit cell is five times that of Cu and Mo. The relative atom contributions decrease in the order Cu >> Mo > O > N > C> H in the VB contributions (Table S3), and in the order Mo >> Cu > N > C > O> H in the CB contributions (Table S3). These findings show that the SHG of  $CuMoO_3(p2c)$  is governed largely by the occupied states of Cu 3d, Mo4p, and O 2p, and by the unoccupied states of Mo 4d, Cu 3d, and N-2p. The metal atoms Cu and Mo contribute much more strongly than do the nonmetal atoms in determining the strength of the SHG response in  $CuMoO_3(p2c)$ , which is quite special among the NLO materials known to date.

Symmetry **2022**, 14, 824 8 of 11

**Table 1.** Contributions of the atoms to the largest components of the SHG tensors  $d_{11}$  of CuMoO<sub>3</sub>(p2c).  $N_A$  refers to the number of the atom type (on the same Wyckoff site) in a unit cell;  $A_{\tau}$ ,  $N_A A_{\tau}$ ,  ${}^{VB} A_{\tau}$ ,  ${}^{CB} A_{\tau}$  refer to the contributions (in %) from a single atom, the total atoms of the same type, all VBs for a single atom, and all CBs for a single atom, respectively.  $d_{\tau}$  denotes the actual value of the contribution (in pm/V) to the SHG for a single atom.

Atom	$N_{\mathbf{A}}$	$A_{ au}$	$^{VB}A_{ au}$	$^{\it CB}A_{ au}$	$N_{ m A}A_{ au}$	$d_{\tau}$
Cu	3	11.72	10.69	1.03	35.2	3.99
Mo	3	6.97	2.85	4.12	20.9	2.38
O	15	1.6	1.14	0.46	24.1	0.55
N	6	1.23	0.51	0.72	7.4	0.42
C	15	0.74	0.27	0.47	11.1	0.25
Н	9	0.15	0.05	0.1	1.4	0.05

According to the individual atomic contribution to the SHG response, the contribution of an atomic group can be calculated by summing the contributions of the center atom and those of its ligands. In this work, we partition the contribution of an anion ( $O^{2-}$  and  $N^{3-}$ ) equally to all the atomic groups it belongs to. The contribution of an atomic group can be calculated by summing the contributions of the center atom and those of its coordinated atoms [55]. Considering the coordination number for each O and N atom (2 and 3, respectively, Figure S8), the group  $CuO_3N$  can be rewritten as  $CuO2_{1/2}O3_{1/2}O5_{1/2}N2_{1/3}$ . Therefore, the group contribution of  $CuO_3N$  to SHG response is calculated as follows,

$$\chi_{[\text{CuO}_3\text{N}]}^{(2)} = \chi_{\text{Cu}}^{(2)} + 1 \times \left(\chi_{\text{O2}}^{(2)} \middle/ 2\right) + 1 \times \left(\chi_{\text{O3}}^{(2)} \middle/ 2\right) + 1 \times \left(\chi_{\text{O5}}^{(2)} \middle/ 2\right) + 1 \times \left(\chi_{\text{N2}}^{(2)} \middle/ 3\right)$$
(6)

The group with anion coordination numbers and the total group contributions for the largest SHG component  $d_{11}$  of CuMoO<sub>3</sub>(p2c) are given in Figure 4, which shows that the metal-centered group [CuO<sub>3</sub>N] and [MoO<sub>5</sub>N] contribute much more strongly to the SHG response than does the organic p2c ligand. That is, the total contribution of the inorganic part is ~79.1%, which far surpasses that of the organic part (i.e., ~20.9%). Our results reflect that the inorganic part contributes dominantly to the SHG response, while the organic part is important in the stabilization of the crystal structure of CuMoO<sub>3</sub>(p2c). It is worth mentioning that we did not separately calculate the hyperpolarizability tensor  $\beta_{ijk}$  by cutting out the ligand or groups from the structure of the compound. Such an approach will unavoidably lead to uncontrolled errors; thus, they are not used in our calculations.

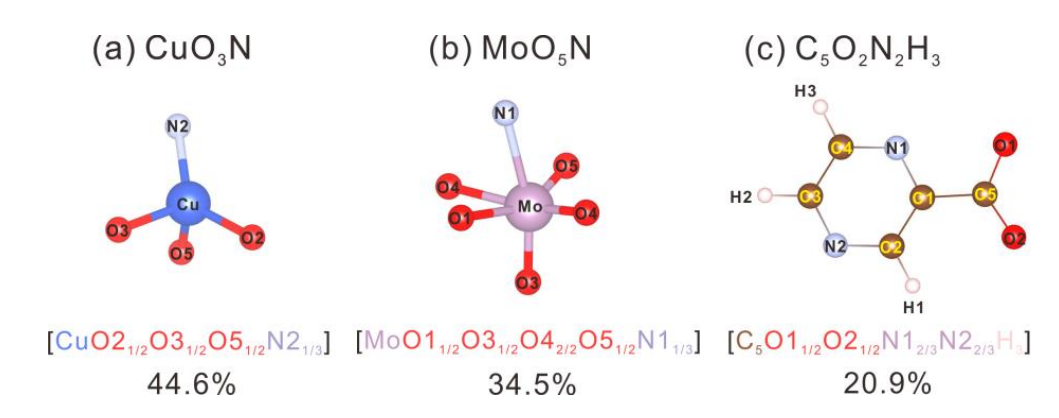


**Figure 4.** The cause for the large second harmonic generation (SHG) of the metal-oxide/organic hybrid compound  $CuMoO_3(p2c)$  is shown to be the inorganic metal-cation-centered groups  $[CuO_3N]$  and  $[MoO_5N]$  rather than the organic nonmetal-cation-centered groups  $[C_5O_2N_2H_3]$ .

Symmetry **2022**, 14, 824 9 of 11

#### 4. Conclusions

Although a number of NCS HF materials with 3D and 2D frameworks have been reported with large SHG response, only low SHG intensities have been measured for HF materials with 1D helical chains. Our first-principles calculations predict that the recently synthesized  $CuMoO_3(p2c)$  exhibits the largest SHG response among all the NCS HF materials with 1D helical chains. Its static effective SHG response, 30.6 pm/V, is about 3.12 times greater than that of commercial AGS, and 92.7 times greater than that of KDP. This value also exceeds those of most NCS hybrid framework materials reported so far. Our ART analysis shows that the SHG of  $CuMoO_3(p2c)$  is determined largely by the occupied states composed of Cu 3d, Cu 3d, and Cu 4d, Cu 3d, and Cu 5d, and Cu

Supplementary Materials: The following are available online at https://www.mdpi.com/article/10 .3390/sym14040824/s1, Figure S1: Calculated band structure for P32-CuMoO3(p2c). Figure S2: HOMO (M<sub>1</sub>) and LUMO (A<sub>1</sub>) for CuMoO<sub>3</sub>(p2c). Figure S3: Calculated partial DOS for P3<sub>2</sub>-CuMoO<sub>3</sub>(p2c). Figure S4: Calculated partial DOS of O and N atoms at independent crystallographic positions. Figure S5: Frequency-dependent refractive indices n (left) and birefringence  $\Delta n$  (right) of CuMoO<sub>3</sub>(p2c). Figure S6: (a)  $\delta \zeta_V(E_B)$ -vs- $E_B$  plot, and (b)  $\delta \zeta_C(E_B)$ -vs- $E_B$  plot calculated for the SHG coefficient  $d_{11}$  of CuMoO<sub>3</sub>(p2c). The values of the functions are in pm/V. Figure S7: Plots of (a)  $\zeta_V(I_B)$ -vs- $I_B$ , (b)  $\zeta_C(I_B)$ -vs- $I_B$ , (c)  $\delta\zeta_V(I_B)$ -vs- $I_B$  and (d)  $\delta\zeta_C(I_B)$ -vs-IB calculated for the SHG coefficient d11 of CuMoO3(p2c). The values of the functions are in pm/V. Figure S8: Coordination environment for each inequivalent O and N atom of CuMoO3(p2c). Table S1: The optimized crystal structure data for  $P3_2$ -CuMoO<sub>3</sub>(p2c). Table S2: Calculated SHG tensors  $d_{i1}$  and  $d_{eff}^{\nu}$  for CuMoO<sub>3</sub>(p2c) and several NCS HF compounds with helical chains. For the compounds with no available experimental band gap ( $E_{\rm g}$ ), the calculated  $E_{\rm g}$  based on HSE06 with mixing parameter  $\alpha$  = 0.3 is applied. The available experimental measured SHG responses are also presented. In this work, Kleinman symmetry is not enforced in calculating the NLO properties. Table S3: Contributions of the individual atoms to the SHG component  $d_{11}$  of CuMoO<sub>3</sub>(p2c). W<sub>A</sub> refers to the number of the same type of atoms (on the same Wyckoff site) in a unit cell.  $A_{\tau}$  is the contribution (in %) from a single atom  $\tau$ , and  $C_A$  from all atoms of the same type.  $V^B A_{T_i}$  is the contribution (in %) the VBs, and  $C^B A_{T_i}$  from the CBs. The contributions from the s, p, and d states of the atom  $\tau$  to of  ${}^{VB}A_{\tau}$  and  ${}^{CB}A_{\tau}$  are also shown [56,57].

**Author Contributions:** Conceptualization, X.C., M.-H.W. and S.D.; methodology, X.C.; software, X.C. and C.L.; validation, X.C., T.Y. and X.H.; formal analysis, X.C., T.Y., X.H., M.-H.W. and S.D.; investigation, X.C., C.L. and P.A.M.; resources, P.A.M. and S.D.; data curation, X.C., T.Y and X.H; writing—original draft preparation, X.C.; writing—review and editing, X.C., T.Y., X.H., C.L., P.A.M., M.-H.W. and S.D.; visualization, X.C.; supervision, M.-H.W. and S.D.; project administration, M.-H.W. and S.D.; funding acquisition, X.C., P.A.M., M.-H.W. and S.D. All authors have read and agreed to the published version of the manuscript.

**Funding:** This research was funded by the National Natural Science Foundation (NSF) of China (22031009, 21921001, 22075282, 61874122); the National Key Research and Development Program of China (2021YFB3601501); the NSF of Fujian Province (2019J05151, 2019J01121); the Youth Innovation Promotion of CAS (2019302); the Fujian Science & Technology Innovation Laboratory for Optoelectronic Information of China (2021ZR123); President's International Fellowship Initiative of CAS (2019VMA0049). P.A.M. acknowledges support from the National Science Foundation (DMR-2004455).

Institutional Review Board Statement: Not applicable.

**Informed Consent Statement:** Not applicable.

**Data Availability Statement:** The data presented in this study are available in the article and supplementary material.

Symmetry **2022**, 14, 824 10 of 11

#### **Conflicts of Interest:** The authors declare no conflict of interest.

## References

- 1. Shen, Y.R. The Principles of Nonlinear Optics; Wiley-Interscience: New York, NY, USA, 1984.
- 2. Chen, C.T.; Sasaki, T.; Li, R.; Wu, Y.; Lin, Z.; Mori, Y.; Kaneda, Y. *Nonlinear Optical Borate Crystals*; Wiley-VCH: Weinheim, Germany, 2012.
- Chung, I.; Kanatzidis, M.G. Metal Chalcogenides: A Rich Source of Nonlinear Optical Materials. Chem. Mater. 2014, 26, 849–869.
   [CrossRef]
- Hu, C.-L.; Mao, J.-G. Recent Advances on Second-Order NLO Materials Based on Metal Iodates. Coor. Chem. Rev. 2015, 288, 1–17.
   [CrossRef]
- 5. Ok, K.M. Toward the Rational Design of Novel Noncentrosymmetric Materials: Factors Influencing the Framework Structures. *Acc. Chem. Res.* **2016**, *49*, 2774–2785. [CrossRef] [PubMed]
- 6. Evans, O.R.; Lin, W. Crystal Engineering of NLO Materials Based on Metal-Organic Coordination Networks. *Acc. Chem. Res.* **2002**, *35*, 511–522. [CrossRef]
- 7. Maury, O.; Bozec, H.L. Molecular Engineering of Octupolar NLO Molecules and Materials Based on Bipyridyl Metal Complexes. *Acc. Chem. Res.* **2005**, *38*, 691–704. [CrossRef]
- 8. Wang, C.; Zhang, T.; Lin, W. Rational Synthesis of Noncentrosymmetric Metal-Organic Frameworks for Second-Order Nonlinear Optics. *Chem. Rev.* **2012**, *112*, 1084–1104. [CrossRef]
- 9. Mingabudinova, L.R.; Vinogradov, V.V.; Milichko, V.A.; Hey-Hawkins, E.; Vinogradov, A.V. Metal-Organic Frameworks as Competitive Materials for Non-Linear Optics. *Chem. Soc. Rev.* **2016**, *45*, 5408–5431. [CrossRef]
- 10. Medishetty, R.; Zareba, J.K.; Mayer, D.; Samoc, M.; Fischer, R.A. Nonlinear Optical Properties, Upconversion and Lasing in Metal-Organic Frameworks. *Chem. Soc. Rev.* **2017**, *46*, 4976–5004. [CrossRef]
- 11. Furukawa, H.; Cordova, K.E.; O'Keeffe, M.; Yaghi, O.M. The Chemistry and Applications of Metal-Organic Frameworks. *Science* **2013**, *341*, 1230444. [CrossRef]
- 12. Zhou, H.C.; Kitagawa, S. Metal-Organic Frameworks (MOFs). Chem. Soc. Rev. 2014, 43, 5415–5418. [CrossRef]
- 13. Cui, Y.; Li, B.; He, H.; Zhou, W.; Chen, B.; Qian, G. Metal-Organic Frameworks as Platforms for Functional Materials. *Acc. Chem. Res.* **2016**, *49*, 483–493. [CrossRef] [PubMed]
- 14. Evans, O.R.; Lin, W. Rational Design of Nonlinear Optical Materials Based on 2D Coordination Networks. *Chem. Mater.* **2001**, *13*, 3009–3017. [CrossRef]
- 15. Lin, W.; Wang, Z.; Ma, L. A Novel Octupolar Metalorganic NLO Material Based on a Chiral 2D Coordination Network. *J. Am. Chem. Soc.* **1999**, *121*, 11249–11250. [CrossRef]
- 16. Ye, Q.; Li, Y.H.; Song, Y.M.; Huang, X.F.; Xiong, R.G.; Xue, Z. A Second-Order Nonlinear Optical Material Prepared Through in situ Hydrothermal Ligand Synthesis. *Inorg. Chem.* **2005**, *44*, 3618–3625. [CrossRef] [PubMed]
- 17. Yu, J.; Cui, Y.; Wu, C.; Yang, Y.; Wang, Z.; O'Keeffe, M.; Chen, B.; Qian, G. Second-Order Nonlinear Optical Activity Induced by Ordered Dipolar Chromophores Confined in the Pores of an Anionic Metal-Organic Framework. *Angew. Chem. Int. Ed.* **2012**, *51*, 10542–10545. [CrossRef]
- 18. Maggard, P.A.; Stern, C.L.; Poeppelmeier, K.R. Understanding the Role of Helical Chains in the Formation of Noncentrosymmetric Solids. *J. Am. Chem. Soc.* **2001**, 123, 7742–7743. [CrossRef]
- 19. Maggard, P.A.; Kopf, A.L.; Stern, C.L.; Poeppelmeier, K.R. From Linear Inorganic Chains to Helices: Chirality in the M(pyz)(H<sub>2</sub>O)<sub>2</sub>MoO<sub>2</sub>F<sub>4</sub> (M)=Zn, Cd) Compounds. *Inorg. Chem.* **2002**, *41*, 4852–4858. [CrossRef]
- 20. Yan, B.; Capracotta, M.D.; Maggard, P.A. Structural Origin of Chirality and Properties of a Remarkable Helically Pillared Solid. *Inorg. Chem.* **2005**, 44, 6509–6511. [CrossRef]
- 21. Ahmed, B.; Jo, H.; Oh, S.J.; Ok, K.M. Variable Asymmetric Chains in Transition Metal Oxyfluorides: Structure-Second-Harmonic-Generation Property Relationships. *Inorg. Chem.* **2018**, *57*, 6702–6709. [CrossRef]
- 22. Muller, E.A.; Cannon, R.J.; Sarjeant, A.N.; Ok, K.M.; Halasyamani, P.S.; Norquist, A.J. Directed Synthesis of Noncentrosymmetric Molybdates. *Cryst. Growth Des.* **2005**, *5*, 1913–1917. [CrossRef]
- 23. Luo, L.; Chen, Y.; Maggard, P.A. Rare Example of Chiral and Achiral Polymorphs of a Metal-Oxide/Organic Hybrid Compound. *J. Solid State Chem.* **2020**, *287*, 121358. [CrossRef]
- 24. Cheng, X.; Whangbo, M.-H.; Guo, G.-C.; Hong, M.; Deng, S. Large Second Harmonic Generation of LiCs<sub>2</sub>PO<sub>4</sub> Caused by the Metal-Cation-Centered Groups. *Angew. Chem. Int. Ed.* **2018**, *57*, 3933–3937. [CrossRef] [PubMed]
- 25. Hohenberg, P.; Kohn, W. Inhomogeneous Electron Gas. Phys. Rev. 1964, 136, B864–B871. [CrossRef]
- 26. Kohn, W.; Sham, L.J. Self-Consistent Equations Including Exchange and Correlation Effects. *Phys. Rev.* **1965**, *140*, A1133–A1138. [CrossRef]
- 27. Kresse, G.; Hafner, J. Ab initio Molecular Dynamics for Liquid Metals. Phys. Rev. B 1993, 47, 558–561. [CrossRef]
- 28. Kresse, G.; Furthmüller, J. Efficiency of *ab-initio* Total Energy Calculations for Metals and Semiconductors Using a Plane-Wave Basis Set. *Comput. Mat. Sci.* **1996**, *6*, 15–50. [CrossRef]
- 29. Kresse, G.; Furthmüller, J. Efficient Iterative Schemes for ab initio Total-Energy Calculations Using a Plane-Wave Basis Set. *Phys. Rev. B* **1996**, *54*, 11169–11186. [CrossRef]
- 30. Blöchl, P.E. Projector Augmented-Wave Method. Phys. Rev. B 1994, 50, 17953-17979. [CrossRef]

Symmetry 2022, 14, 824 11 of 11

31. Perdew, J.P.; Burke, K.; Ernzerhof, M. Generalized Gradient Approximation Made Simple. *Phys. Rev. Lett.* **1996**, *77*, 3865–3868. [CrossRef]

- 32. Perdew, J.P.; Wang, Y. Accurate and Simple Analytic Representation of the Electron-Gas Correlation Energy. *Phys. Rev. B* **1992**, 45, 13244–13249. [CrossRef]
- 33. Aversa, C.; Sipe, J.E. Nonlinear Optical Susceptibilities of Semiconductors: Results with a Length-Gauge Analysis. *Phys. Rev. B* **1995**, 52, 14636–14645. [CrossRef] [PubMed]
- 34. Rashkeev, S.N.; Lambrecht, W.R.; Segall, B. Efficient ab initio Method for the Calculation of Frequency-Dependent Second-Order Optical Response in Semiconductors. *Phys. Rev. B* **1998**, *57*, 3905–3919. [CrossRef]
- 35. Sharma, S.; Ambrosch-Draxl, C. Second-Harmonic Optical Response from First Principles. *Phys. Scripta* **2004**, *T109*, 128–134. [CrossRef]
- 36. Rashkeev, S.N.; Lambrecht, W.R.L. Second-Harmonic Generation of I-III-VI<sub>2</sub> Chalcopyrite Semiconductors: Effects of Chemical Substitutions. *Phys. Rev. B* **2001**, *63*, 165212. [CrossRef]
- 37. Sharma, S.; Dewhurst, J.K.; Ambrosch-Draxl, C. Linear and Second-Order Optical Response of III-V Monolayer Superlattices. *Phys. Rev. B* **2003**, *67*, 165332. [CrossRef]
- 38. Cheng, X.; Whangbo, M.-H.; Hong, M.; Deng, S. Atom Response Theory of Nonlinear Optical Responses and Its Applications. *Chinese J. Struct. Chem.* **2020**, *39*, 2172–2181. [CrossRef]
- 39. Sioncke, S.; Verbiest, T.; Persoons, A. Second-Order Nonlinear Optical Properties of Chiral Materials. *Mater. Sci. Eng. R* **2003**, 42, 115–155. [CrossRef]
- 40. Gonze, X.; Lee, C. Dynamical Matrices, Born Effective Charges, Dielectric Permittivity Tensors, and Interatomic Force Constants from Density-Functional Perturbation Theory. *Phys. Rev. B* **1997**, *55*, 10355–10368. [CrossRef]
- 41. Veithen, M.; Gonze, X.; Ghosez, P. Nonlinear Optical Susceptibilities, Raman Efficiencies, and Electro-Optic Tensors from First-Principles Density Functional Perturbation Theory. *Phys. Rev. B* **2005**, *71*, 125107. [CrossRef]
- 42. Djani, H.; Hermet, P.; Ghosez, P. First-Principles Characterization of the *P*2<sub>1</sub>*ab* Ferroelectric Phase of Aurivillius Bi<sub>2</sub>WO<sub>6</sub>. *J. Phys. Chem. C* **2014**, *118*, 13514–13524. [CrossRef]
- 43. Dronskowski, R.; Bloechl, P.E. Crystal orbital Hamilton populations (COHP): Energy-resolved visualization of chemical bonding in solids based on density-functional calculations. *J. Phys. Chem.* **1993**, *97*, 8617–8624. [CrossRef]
- 44. Deringer, V.L.; Tchougreeff, A.L.; Dronskowski, R. Crystal Orbital Hamilton Population (COHP) Analysis as Projected from Plane-Wave Basis Sets. *J. Phys. Chem. A* **2011**, *115*, 5461–5466. [CrossRef] [PubMed]
- 45. Kurtz, S.K.; Perry, T.T. A Powder Technique for the Evaluation of Nonlinear Optical Materials. *J. Appl. Phys.* **1968**, 39, 3798–3813. [CrossRef]
- 46. Cyvin, S.J.; Rauch, J.E.; Decius, J.C. Theory of Hyper-Raman Effects (Nonlinear Inelastic Light Scattering): Selection Rules and Depolarization Ratios for the Second-Order Polarizability. *J. Chem. Phys.* **1965**, *43*, 4083–4095. [CrossRef]
- 47. Midwinter, J.E.; Warner, J. The Effects of Phase Matching Method and of Uniaxial Crystal Symmetry on the Polar Distribution of Second-Order Non-Linear Optical Polarization. *Br. J. Appl. Phys.* **1965**, *16*, 1135–1142. [CrossRef]
- 48. Astill, A.G. Material Figures of Merit for Non-Linear Optics. Thin Solid Films 1991, 204, 1–17. [CrossRef]
- 49. Ye, Q.; Tang, Y.Z.; Wang, X.S.; Xiong, R.G. Strong Enhancement of Second-Harmonic Generation (SHG) Response Through Multi-Chiral Centers and Metal-Coordination. *Dalton Trans.* **2005**, *9*, 1570–1573. [CrossRef]
- 50. Lin, W.; Evans, O.R.; Xiong, R.G.; Wang, Z. Supramolecular Engineering of Chiral and Acentric 2d Networks. Synthesis, Structures, and Second-Order Nonlinear Optical Properties of Bis(nicotinato)zinc and Bis{3-[2-(4-pyridyl)ethenyl]benzoatocadmium. *J. Am. Chem. Soc.* 1998, 120, 13272–13273. [CrossRef]
- 51. Liu, B.W.; Jiang, X.M.; Li, B.X.; Zeng, H.Y.; Guo, G.C. Li[LiCs<sub>2</sub>Cl][Ga<sub>3</sub>S<sub>6</sub>]: A Nanoporous Framework of GaS<sub>4</sub> Tetrahedra with Excellent Nonlinear Optical Performance. *Angew. Chem. Int. Ed.* **2020**, *59*, 4856–4859. [CrossRef]
- 52. Li, R.A.; Zhou, Z.; Lian, Y.K.; Jia, F.; Jiang, X.; Tang, M.C.; Wu, L.M.; Sun, J.; Chen, L. A<sub>2</sub>SnS<sub>5</sub>: A Structural Incommensurate Modulation Exhibiting Strong Second-Harmonic Generation and a High Laser-Induced Damage Threshold (*A* = Ba, Sr). *Angew. Chem. Int. Ed.* **2020**, *59*, 11861–11865. [CrossRef]
- 53. Ye, R.; Cheng, X.; Liu, B.-W.; Jiang, X.-M.; Yang, L.-Q.; Deng, S.; Guo, G.-C. Strong Nonlinear Optical Effect Attained by Atom-Response-Theory Aided Design in the Na<sub>2</sub> $M^{II}M^{IV2}Q_6$  ( $M^{II}$  = Zn, Cd;  $M^{IV}$  = Ge, Sn; Q = S, Se) Chalcogenide System. *J. Mater. Chem. C* **2020**, *8*, 1244–1247. [CrossRef]
- 54. Guo, S.-P.; Cheng, X.Y.; Sun, Z.D.; Chi, Y.; Liu, B.W.; Jiang, X.M.; Li, S.F.; Xue, H.G.; Deng, S.; Duppel, V.; et al. Large SHG Effect and High LIDT Observed Coexisting in Gallium Selenide: A Simple but Perfect Case. *Angew. Chem. Int. Ed.* **2019**, *131*, 8171–8175. [CrossRef]
- 55. Cai, Z.; Cheng, X.; Whangbo, M.-H.; Hong, M.; Deng, S. The Partition Principles for Atom Scale Structure and its Physical Property: Application to the Nonlinear Optical Crystal Material KBe<sub>2</sub>BO<sub>3</sub>F<sub>2</sub>. *Phys. Chem. Chem. Phys.* **2020**, 22, 19299–19306. [CrossRef]
- 56. Lin, H.; Maggard, P.A. Copper(i)-rhenate hybrids: Syntheses, structures, and optical properties. *Inorg. Chem.* **2007**, *46*, 1283–1290. [CrossRef] [PubMed]
- 57. Gautier, R.; Poeppelmeier, K. Packing of Helices: Is Chirality the Highest Crystallographic Symmetry? *Crystals* **2016**, *6*, 106. [CrossRef]